Boosting energy storage performance in $Ba_{0.8}Sr_{0.2}Zr_{0.1}Ti_{0.9}O_3$–$Na_{0.5}Bi_{0.5}TiO_3$ lead-free nanoceramics through polar nanoregions and grain refinement engineering

Run Zhang[1], Lili Zhao[2], Zhi'ang Zhang[2], Xiaoting Zhang[1], Quan Jin[1], and Bin Cui[1,*] (ID)

[1] *Key Laboratory of Synthetic and Natural Functional Molecule of Ministry of Education, Shaanxi Key Laboratory of Physico-Inorganic Chemistry, College of Chemistry & Materials Science, Northwest University, 1 Xuefu Ave., Chang'an District, Xi'an 710127, Shaanxi, China*
[2] *School of Information Science and Technology, Northwest University, Xi'an 710127, Shaanxi, China*

ABSTRACT

Polar nanoregions and grain refinement engineering are alternative methods to develop comprehensive energy storage performance ceramic materials. In our work, $Ba_{0.8}Sr_{0.2}Zr_{0.1}Ti_{0.9}O_3$ (BSZT) and $Na_{0.5}Bi_{0.5}TiO_3$ (NBT) powders with average particle sizes of 200 nm and 50 nm were fabricated by a wet chemical method and BSZT-xNBT (x = 0, 0.02, 0.04, 0.06, 0.08 wt%) ceramic samples were prepared by utilizing the two powders. The systematic study confirmed that pure BSZT ceramics possessed pseudocubic phase, and the coexistence of tetragonal phase (T) and rhombic phase (R) was observed at x = 0.06. PFM and TEM examinations revealed that the domain structure of BSZT-0.06NBT ceramics had transformed from ferroelectric domains into polar nanoregions. Additionally, the sintering behavior of ceramics could be effectively improved by the addition of NBT with small particle size, and the dense fine-grained ceramics with 198 nm were obtained when the NBT amount reached up to 0.06. BSZT-0.06NBT ceramics sintered at 980 °C exhibit a high dielectric constant of 3620 and a low dielectric loss of 0.02 at Curie temperature. Ferroelectric hysteresis loops become slimmer and slimmer with the increased x, which may be ascribed to the enhancement of relaxor behavior and domain transition in the ceramics. For the composition of x = 0.06, the maximum energy storage density of 1.72 J cm^{-3} and a moderate energy storage efficiency of 78.2% were realized under 18.32 kV mm^{-1}. This work suggests that BSZT-0.06NBT relaxor ferroelectric ceramics are expected to be applied in the energy storage field.

Address correspondence to E-mail: cuibin@nwu.edu.cn

1 Introduction

Bulk ceramic dielectric capacitors are critically important in the electric power systems due to their excellent environmental adaptability, extraordinary electrical properties, and ultra-fast charge and discharge rates [1, 2]. Nevertheless, the energy storage application is always restricted by their low energy storage density. In essence, the energy storage density is decided by a combination of the polarization ability (ΔP) and breakdown field strength (BDS) [3], researchers are mainly engaged in developing the ceramic materials with large ΔP and high BDS.

BaTiO$_3$ is considered as the most promising candidate in the energy storage application, which could be ascribed to the strong spontaneous polarization resulting from the displacement of Ti^{4+} ions along the inner axis of the TiO$_6$ octahedron. However, pristine BaTiO$_3$ displays large remnant polarization (P_r), low BDS, and low energy storage density [4]. The improvement of energy storage performance is usually achieved by the substitution of foreign ions at A and B sites [5]. It has been reported that the weak coupling effect of A-site ions and B-site ions caused by doping can produce domain reverse, lattice transformation, and crystal deformation under the stimulation of an applied electric field [6]. For example, the substitution of Zr^{4+} for Ti^{4+} leads to a lattice expansion, which generates the distortion of the TiO$_6$ octahedron and induces a strong spontaneous polarization [7]. The substitution of Sr^{2+} ions is well known to disrupt the long-range order of BaTiO$_3$ ferroelectrics, and promote the formation of relaxor state, improving the hysteresis [8]. Based on the above consideration, lots of studies focused on the modified Ba$_{0.8}$Sr$_{0.2}$Zr$_{0.1}$Ti$_{0.9}$O$_3$ systems [9–11]. However, the low energy storage density (usually less than 1.0 J cm^{-3}) of final ceramics owning to low BDS (usually less than 150 kV cm^{-1}) and small ΔP value (probably less than 10 μC cm^{-2}) constricts their application in energy storage capacitors.

Fortunately, recent studies have shown that the ΔP value of ceramic materials could be enhanced through polar nanoregions engineering [12–14]. Through doping and solid solution, polar nanoregions can be formed due to the local component heterogeneity and the interface polarization [15]. The last decade has witnessed the development of dielectric materials including BiFeO$_3$ (BF), K$_{0.5}$Na$_{0.5}$NbO$_3$ (KNN), Na$_{0.5}$Bi$_{0.5}$TiO$_3$ (NBT), and BaTiO$_3$-based ceramics. For BF ceramics, although its saturation polarization (P_m) is as high as 80 μC cm^{-2}, it usually has a large leakage current [16]. For KNN ceramics, it is difficult to prepare dense ceramics without special sintering process [17]. For NBT ceramics, a kind of perovskite-type ferroelectrics with A-site composite ions, it displays rhombohedral phase and ultra-high P_m of 43 μC cm^{-2} [18]. The partial substitution of Na$^+$ and Bi^{3+} at A-site of BaTiO$_3$-based materials would result in a significant improvement of the polarization linearity of ceramic materials. For example, Zouari et al. [19] prepared 0.85Ba$_{0.995}$Pr$_{0.005}$Ti$_{0.9}$Zr$_{0.1}$O$_3$-0.15Na$_{0.5}$Bi$_{0.5}$TiO$_3$ ceramics with core–shell structural grains. The doping of Pr is generally related to the luminescence of materials. Although the author has optimized the polarization linearity of ceramic materials, BDS (only 3 kV mm^{-1}) and ΔP (5 μC cm^{-2}) are quite small, and there is lack of characterization and in-depth analysis about the "core–shell" structure. Wang et al. [20] fabricated $(1 - x)$ Ba(Zr$_{0.2}$Ti$_{0.8}$)O$_{3-x}$Na$_{0.5}$Bi$_{0.5}$TiO$_3$ ceramics and found that the ion inhomogeneity caused by the addition of NBT could break the microndomains with long-range order into nanodomains with short-range order, thereby improving the ceramic polarization linearity.

The approach of grain refinement engineering also provides a solution to powerfully improve BDS in the ferroelectric materials. It is a well-established fact that the average grain size of ceramics has a reverse correlation with the BDS [21]. Relaxor ferroelectric ceramics with dense microstructure and uniform grain size are more likely to have large BDS [22]. For example, Ren et al. [23] refined the grain size of K$_{0.5}$Na$_{0.5}$NbO$_3$ ceramics and increased the ceramic BDS from 120 to 370 kV cm^{-1} by introducing the second component SrZrO$_3$. The decrease of average grain size may be attributed to the fact that Zr^{4+} aggregates at the grain boundaries and inhibits the mobility of the grain boundaries. Sun et al. [24] investigated Ba$_{1-x}$Sm$_{2x/3}$Zr$_{0.15}$Ti$_{0.85}$O$_3$ ceramics and proved that the lattice shrinkage led to the reduced ceramic grain size, and thus the BDS was enhanced. The reason why the grain size of ceramics has an effect on BDS is that the grain refinement increases the percentage of grain boundaries, so that the internal breakdown path will be transformed across from whole ceramic grains to the grain boundary edge [25].

In this paper, we prepared $Ba_{0.8}Sr_{0.2}Zr_{0.1}Ti_{0.9}O_3 - xNa_{0.5}Bi_{0.5}TiO_3$ (BSZT-xNBT, $x = 0$, 0.02, 0.04, 0.06, 0.08 wt%) relaxor ferroelectric ceramics. Figure 1 shows the schematic diagram of optimizing BDS and energy storage properties through the polar nanoregions and grain refinement engineering. The P_m could be guaranteed by the combination of the relaxor ferroelectrics BSZT and the ferroelectrics NBT. Furthermore, hybridization of 6p orbitals of Bi^{3+} and 2p orbitals of O^{2-} similarly increased P_m [26]. Nonequivalent Na^+ and Bi^{3+} replace Ba^{2+} and Sr^{2+} at A-site, which disrupts the long-range dipole and promotes ferroelectric domains to convert to polar nanoregions, thus reducing P_r [27]. Because NBT powders with 50 nm were introduced to prepare the dense fine-grained ceramics materials, the BDS of ceramics can also be increased. Therefore, the ceramics with comprehensive energy storage properties are expected to be obtained. The composition, morphology, and electrical properties of the BSZT-xNBT ($x = 0$, 0.02, 0.04, 0.06, 0.08 wt%) ceramics were systematically investigated.

2 Experimental

2.1 Experimental reagents

The main reagents involved are $Ba(Ac)_2$ (AR, 99%), NaOH (AR, 99.5%), $Bi(NO_3)_3 \cdot 5H_2O$ (AR, 99.0%), $Zr(NO_3)_4 \cdot 5H_2O$ (AR, 99.0%), $Sr(Ac)_2 \cdot 0.5 \cdot H_2O$ (AR, 99.0%), $TiCl_4$ (Industrial grade, 99.5%), $NaNO_3$ (AR, 99.0%), $Ti(OC_4H_9)_4$ (AR, 99.0%), CH_3CH_2OH (AR, 99%).

2.2 Synthesis of powder precursors and ceramic samples

The 200 nm monodisperse BSZT powders were prepared by a co-precipitation method according to our previous work [28, 29]. In order to prepare the powders with high activity and small particle size, we utilized the citrate sol approach to prepare NBT powders [30]. BSZT and NBT powders were ball-milled according to the stoichiometric formula with zirconia balls media in ethanol for 6 h. The dried powders were mixed with 4 wt% PVA solution and pressed into pellets of 8 mm in diameter and 1 mm in thickness under the pressure of 6 MPa. Based on the requirements for dense and fine-grained ceramics, the obtained pellet samples were heated at 500 °C for 1 h to eliminate the binder and then sintered in air atmosphere at 980 °C for 2 h.

2.3 Structure and property characterization

Phase structure of the ceramics was determined using X-ray powder diffraction (XRD, D8 Advance, Bruker, Frankfurt, Germany) in the 2θ range of 20°–70°. Raman spectrometer (HR-800, Jobin, Yvon) was used to characterize the Raman spectra of the ceramics at 100–1000 cm^{-1}. The microstructure of ceramics was observed via scanning electron microscopy (SEM, Quanta-600, FEI, USA) with energy-dispersive spectroscopic (EDS) analysis. The bulk
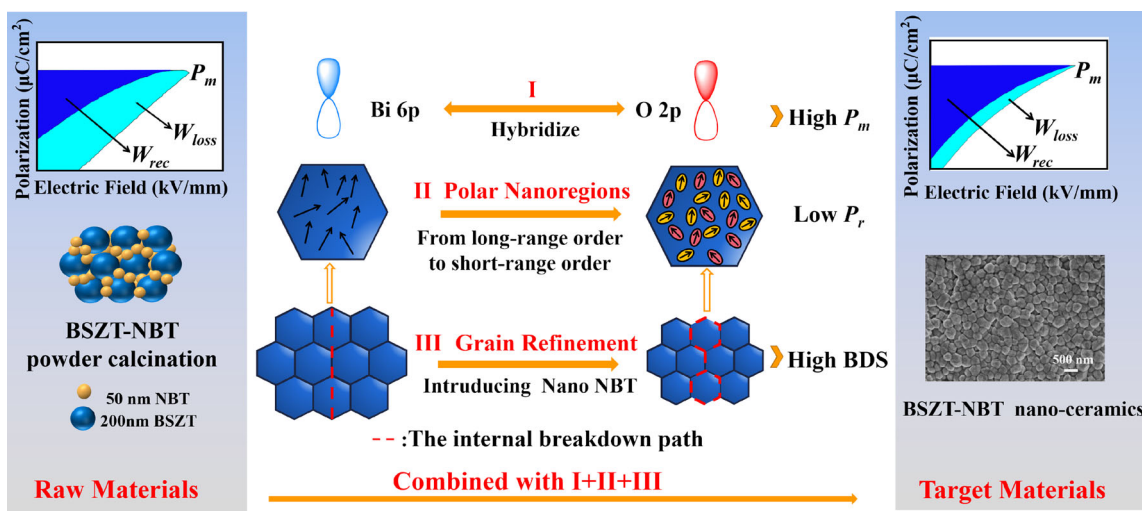

Fig. 1 Schematic figure of optimizing BDS and energy storage properties through the polar nanoregions and grain refinement engineering

densities were measured by the Archimedes' method. The dielectric properties of ceramics were measured by an impedance analyzer (Model HP4284A, Hewlett-Packard, USA) from − 60 to 130 °C at a heating rate of 3 °C min^{-1}. To obtain the unipolar polarization–electric field (P–E) loops, the thickness of the ceramics was polished to 0.3 (± 0.02) mm and characterized by a ferroelectric test system (Model 609B, Radiant technology, Washington, USA). The domain measurements were conducted on a piezoelectric force microscope (PFM, MFP-3D, Asylum Research, USA) analysis and field emission transmission electron microscopy (TEM, Talos F 200X, FEI, USA) with a 5 nm probe. To perform the measurement of PFM, the surface of the samples was polished with silica suspension.

3 Results and discussion

3.1 Effect of NBT amount on the phase composition of BSZT-xNBT ceramics

Figure 2a shows the XRD patterns of BSZT-xNBT ceramics at room temperature. When the doping content is not more than 0.06, the ceramic samples display pure perovskite structure, indicating that NBT has completely diffused into the host lattice of BSZT and formed a homogeneous solid solution [31]. However, the impurities Bi_2O_3 and $Na_{0.45}Bi_{0.5}Ti_4O_{15}$ appear as the doping amount reaches up to 0.08. It can be seen from the enlarged diffraction pattern of 44.8°–45.8° in Fig. 2b and the c/a ratio in Table 1, pure BSZT ceramics show a broad (200) peak of
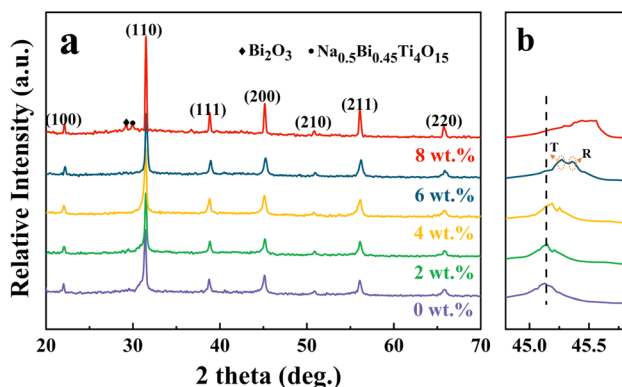

Fig. 2 a XRD patterns of BSZT-xNBT ceramics. **b** Magnified view of 44.8°–45.8° diffraction peaks of the BSZT-xNBT ceramic samples

pseudocubic phase, which is consistent with the literature [32] and has the c/a ratio of 1.0060. When x increases from 2.0 to 6.0 wt%, the (200) peak is disassembled into two peaks, one of which belongs to the T phase, while the other corresponds to the R phase [33]. The T phase gradually becomes inconspicuous, and the R phase increases as x increases. The corresponding c/a ratio decreases gradually. A clear broad peak is presented again in the BSZT-0.08NBT ceramic samples. The corresponding c/a ratio of the BSZT-0.08NBT ceramics is almost equal to 1.0000, suggesting a transition from the state of multiphase coexistence to the pseudocubic phase. At the same time, BSZT-xNBT ceramics diffraction peak (200) shifts to a higher degree with increasing the amount of NBT, which can be explained by the Bragg diffraction formula $2d\sin\theta = n\lambda$. The average ionic radii of $(Na_{0.5}Bi_{0.5})^{2+}$ can be evaluated by the following equation $R = 0.5R(Na^+) + 0.5R(Bi^{3+})$, and the average ion radius of $(Ba_{0.8}Sr_{0.2})^{2+}$ can also be evaluated using the same calculation formula [34]. The above calculation results demonstrate that the average ionic radii of $(Ba_{0.8}Sr_{0.2})^{2+}$ is 138 pm and larger than $(Na_{0.5}Bi_{0.5})^{2+}$ (69 pm) [35]. So, the substitution of Na^+ and Bi^{3+} for Ba^{2+} and Sr^{2+} at A-site induces the diffraction peak (200) shifting to high-angle direction.

As it is well known, Raman spectroscopy is a sensitive method to detect structural transformations with short length scale [36]. The Raman spectra of the BSZT-xNBT ceramics are presented in Fig. 3. From 100 to 1000 cm^{-1}, four common Raman peaks can be detected in the BSZT-xNBT ceramics, which is consistent with other studies [37, 38]. First, the vibration of A-site cations influences the Raman peak around 120 cm^{-1}. The A-site peak tends to flatten gradually. This demonstrated that the formation of the solid solution BSZT-NBT makes A-O dodecahedron distorted, and aggravates the disorder of A-site ions [39]. Secondly, by comparison with other BT-based materials in literature [40], the bands of Ti–O are broadened with NBT addition. Region III during 500–600 cm^{-1} is connected with the vibration of TiO_6 octahedron, a gradual phase transformation occurs with increasing x, as manifested by the appearance of new peaks at 565 cm^{-1} and the decrease of peak value at 515 cm^{-1}. More importantly, the two peaks in Region III indicate the coexistence of T and R phases in the samples with x = 0.06 [41]. Furthermore, the high-frequency bands at 700 cm^{-1} are related to overlapping bands

Table 1 Lattice parameters, bulk densities, and dielectric properties of BSZT-xNBT ceramics sintered at 980 °C

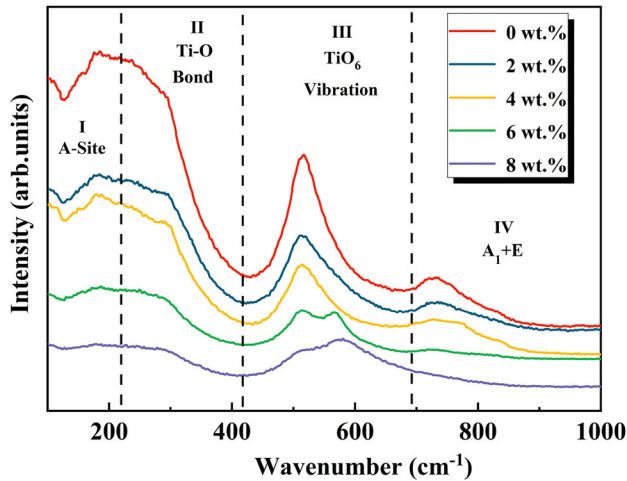| NBT contents (wt%)	a (Å)	c (Å)	c/a	Density (g cm^{-3})	ε_m	tanδ	T_C
0	3.9918	4.0158	1.0060	4.40	1250	0.18	39.4
2	3.9921	4.0151	1.0056	4.68	2290	0.09	48.2
4	3.9987	4.0089	1.0026	4.87	2860	0.06	50.4
6	3.9999	4.0023	1.0008	5.02	3620	0.02	51.0
8	4.0000	4.0013	1.0003	4.98	3217	0.04	52.8

Fig. 3 Raman spectra of the BSZT-xNBT ceramics samples

A_1 (longitudinal optics) and E (longitudinal optics) [42]. Obviously, the Raman peak position shifts towards higher wavenumber direction with increasing x, and the peak gradually widens, confirming that Na^+ and Bi^{3+} have been successfully incorporated into the A-site of BSZT-xNBT ceramics and the long-range ordered T phase becomes disordered. Therefore, the Raman results agree well with the XRD results.

3.2 Effect of NBT amount on the morphology and elements of BSZT-xNBT ceramics

Figure 4a–e show the FESEM images of BSZT-xNBT ceramics obtained with different NBT amount. The dense morphology and the density of 5.02 g cm^{-3} is realized in the BSZT-0.06NBT ceramics. When the doping content is below 0.06, the ceramic grains almost remain unchanged, and then dramatically increase with a further increase in the NBT amount. The grain size change in the ceramic specimens can be ascribed to the following three points. On the one hand, nano-NBT powders with small particle size

form a solid solution with BSZT powders, which results in lattice distortion [43]. On the other hand, nano-NBT powders prepared by the citrate sol approach have large surface energy, high sintering activity, and low sintering temperature. Therefore, Nano-NBT powders evenly distributed around BSZT powders and accelerated the mass transfer so that the sintering temperature of ceramics is sharply reduced to 980 °C [44]. At such an appropriate low sintering temperature, the fine-grained BSZT-xNBT ceramics are obtained [45].

In order to characterize the chemical composition of BSZT-xNBT ceramics, EDS mapping and elemental analysis are performed, as displayed in Fig. 5. It is clear that all elements are uniformly distributed. As illustrated in Fig. 6, the contents of Bi and Na at the grain boundary are significantly higher, confirming that NBT is at the grain boundary, and it did have an obvious effect on the formation of fine-grained dense ceramics at low sintering temperature.

3.3 Effect of NBT amount on the dielectric and energy storage properties of BSZT-xNBT ceramics

Figure 7 shows temperature dependence of the dielectric constant and dielectric loss of the BSZT-xNBT ceramics (measured at 1 kHz) within a temperature range of − 60 °C to 130 °C. As it can be seen from Fig. 7a and b, with the increase of NBT content, the maximum dielectric constants values (ε_m) progressively increase and then decrease, and the dielectric loss decreases first and then increases. It is known that the dielectric properties of ceramics are mainly related to the microstructures. The higher the density the larger ε_m. Furthermore, doping with high polarization ability element is an effective strategy to significantly enhance the dielectric properties of ceramics [46]. Bi^{3+} possesses 6s^2 lone pair electrons, and thus the high polarization ability. Therefore, the introduction of NBT is suggested as the origin of the
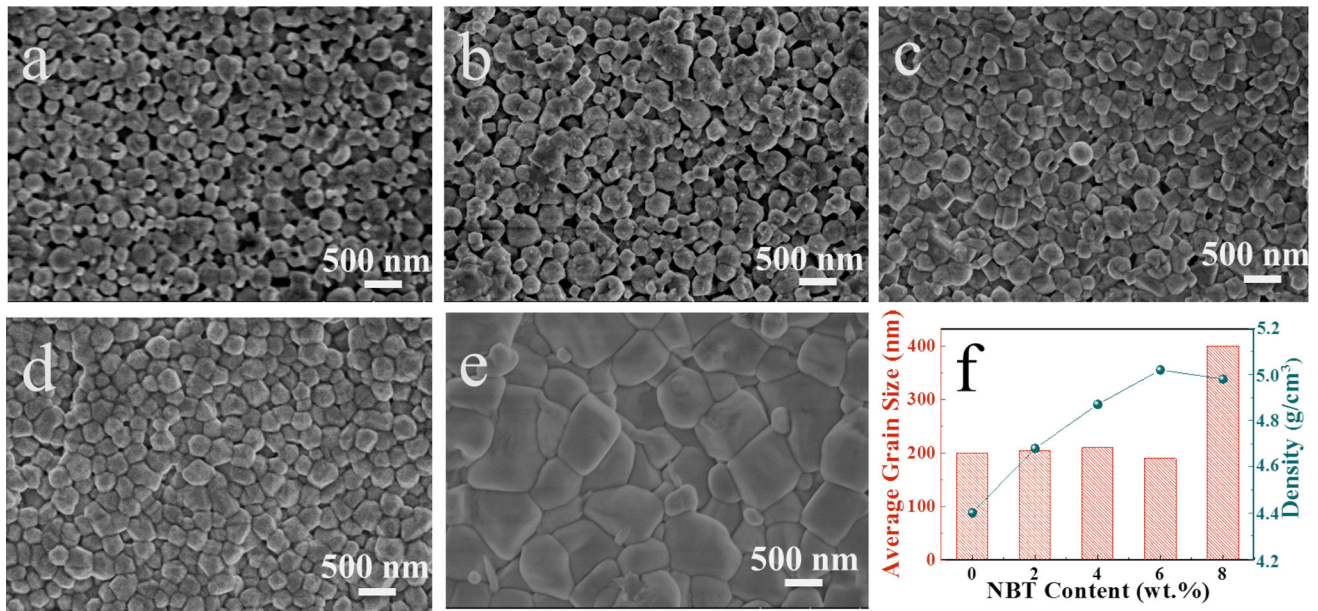
Fig. 4 FESEM micrographs of BSZT-xNBT ceramics with different NBT doping amount: **a** 0 wt%; **b** 2 wt%; **c** 4 wt%; **d** 6 wt%; **e** 8 wt%. **f** The change curve in the average grain size and density of BSZT-xNBT ceramics
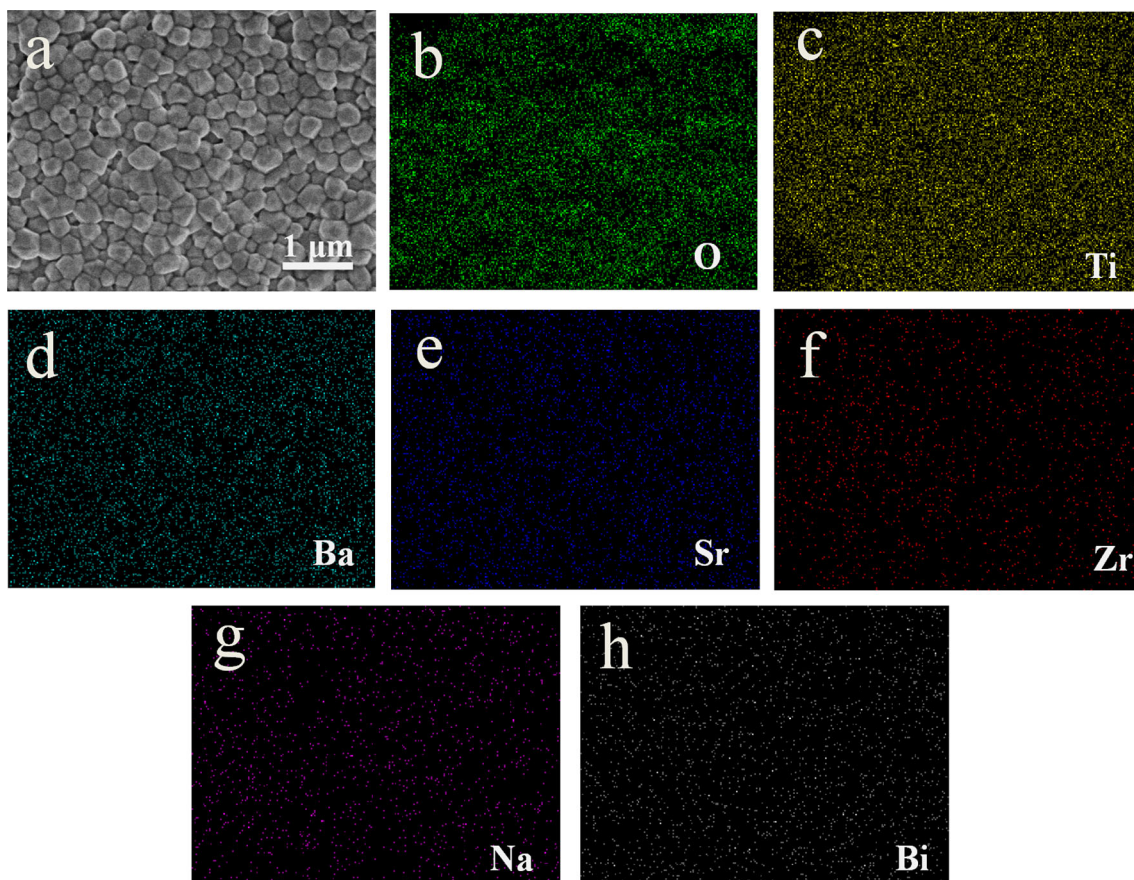

Fig. 5 EDS mapping of BSZT-0.06NBT ceramics

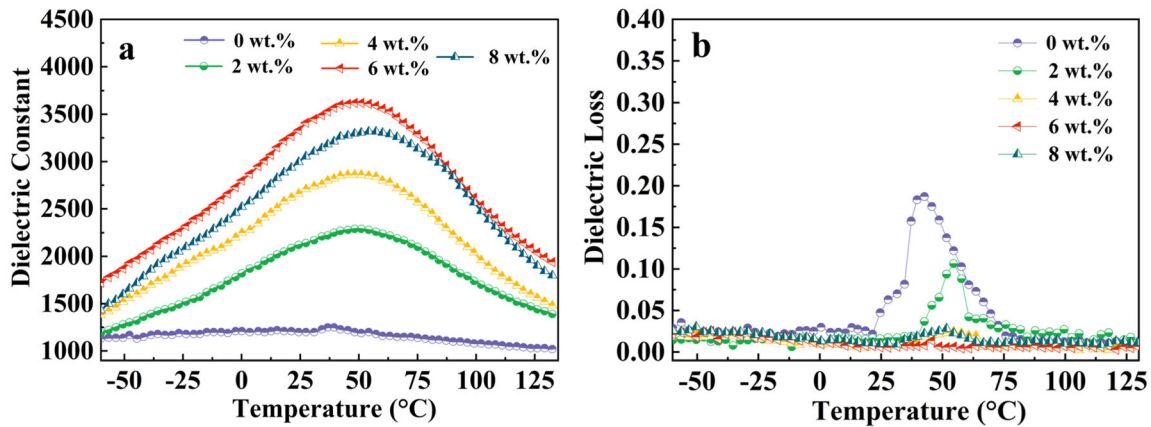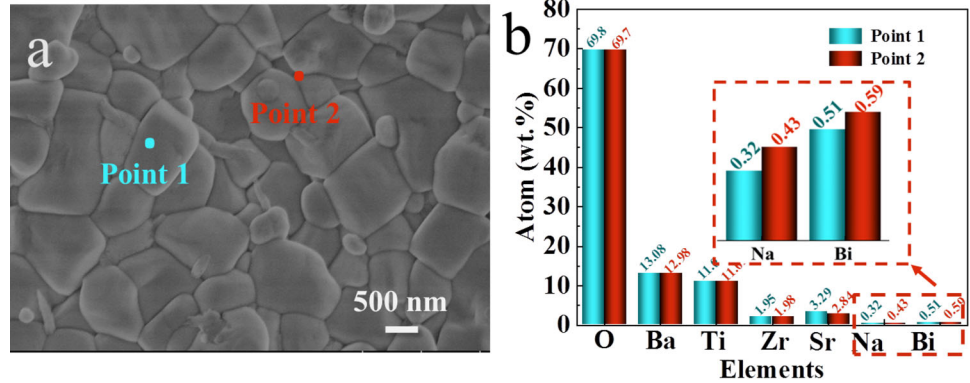Fig. 6 a, b Elements distribution in the grain (Point 1) and grain boundary (Point 2) of BSZT-0.08NBT ceramics

Fig. 7 a Plots of temperature-dependent dielectric constant of BSZT-xNBT ceramics. b Plots of temperature-dependent dielectric loss of BSZT-xNBT ceramics

increased ε_m. The ceramics with dense microstructure are not prone to thermal breakdown and electric breakdown, corresponding to lower dielectric loss. Consequently, the best dielectric properties with the dielectric constant of 3620 and the dielectric loss below 0.02 are obtained in the ceramics with $x = 0.06$. The ferroelectric–paraelectric phase transition temperatures, namely the curie temperature (T_c), increase from 39.4 °C for the pure BSZT ceramics to 48.2 °C, 50.4 °C, 51 °C, and 52.8 °C for the ceramics with $x = 0.02, 0.04, 0.06$, and 0.08, respectively, which is attributed to the increase of solid solubility of NBT in BSZT, strengthening the orientation of spontaneous polarization of TiO_6 octahedron [26]. The dielectric results verify the phase transition in the BSZT-xNBT ceramics, and it is consistent with the above XRD analysis in Fig. 2.

The diffuseness degree (γ) is a critically important parameter to evaluate the relaxor characteristic of ceramics. The values of γ for the BSZT-xNBT ceramics were analyzed by the slope of $\ln(1/\varepsilon - 1/\varepsilon_m)$ versus

$\ln(T - T_m)$ at 1 kHz and depicted in Fig. 8. The inset demonstrates that the calculated γ is 1.84 for $x = 0.06$, indicating a certain degree of relaxor characteristics, which is connected with the local compositional disorder. In this experiment, due to the introduction of nonisovalent Na^+ and Bi^{3+} at A-sites together, the long-range ferroelectric order was disrupted and the short-range dipolar regions were formed [47]. Figure 8a and b show the frequency dependence of dielectric constant and dielectric loss of BSZT-xNBT measured at 25 °C with $x = 0.06$. Figure 8a and b show the frequency dependence of dielectric constant and dielectric loss of BSZT-xNBT measured at 25 °C with $x = 0.06$. Observably, all the samples exhibited typical frequency dispersion and diffuse phase transition. The dielectric peaks become broader and broader with increased frequency. At high frequencies, ε_m drops, and T_m increases. All the above phenomena indicate the diffused ferroelectric phase transition. The increase of dielectric loss with frequency can be attributed to the acceleration of dipole
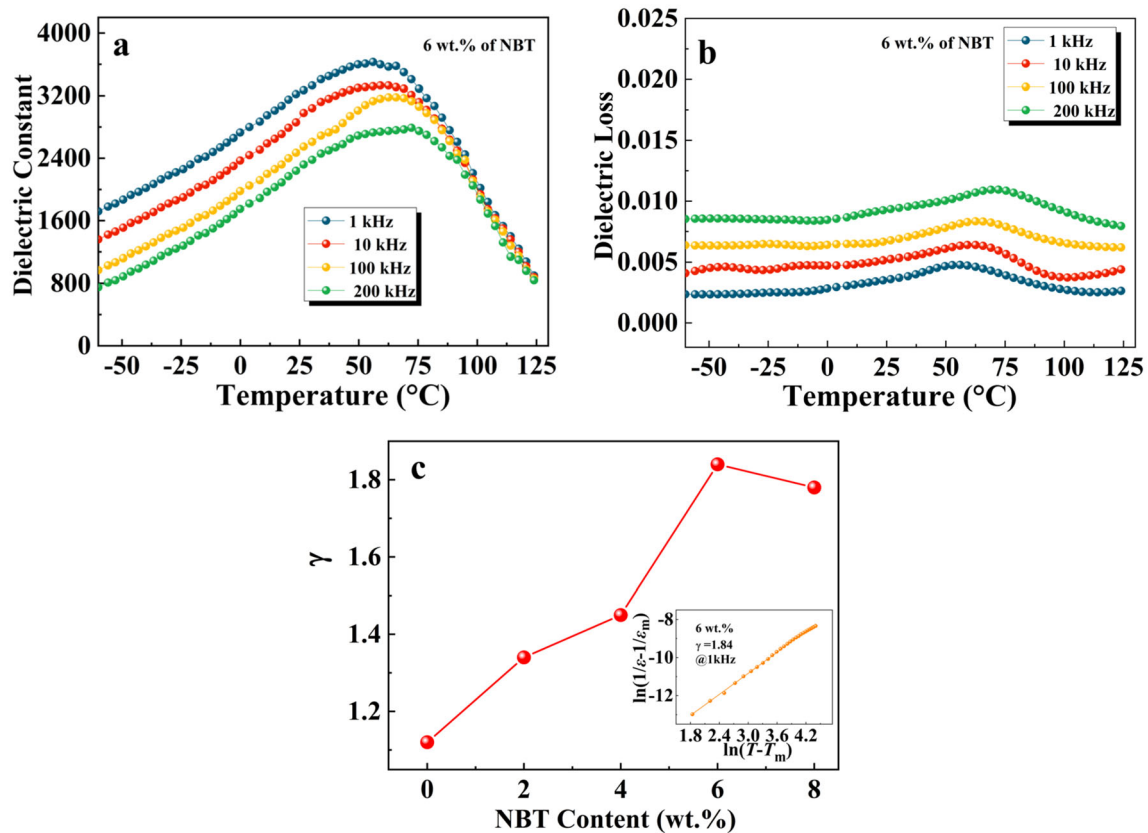
Fig. 8 The γ value change curve fitted by Curie–Weiss law curve at 1 kHz of BSZT-xNBT ceramics. The inset shows $(1/\varepsilon - 1/\varepsilon_m)$ versus $\ln(T - T_m)$ of BSZT-xNBT ceramics with $x = 0.06$

migration at high frequency. Combined with the results of Curie–Weiss law, it is proved that the introduction of nonisovalent Na^+ and Bi^{3+} at A-sites forms polar nanoregions, which results in the phase transition.

The P–E hysteresis loops of BSZT-xNBT ceramics tested at their maximum applied electric field are displayed in Fig. 9. It can be intuitively found that BSZT-0.06NBT ceramic possesses a slimmer P–E hysteresis loop than others. The ΔP value of ceramics gradually raised from 10.00 to 18.25 μC cm^{-2} with an increase in the concentration of the NBT from $x = 0$ to 0.06 as shown in Fig. 9b, which could be related to the long-range dipolar structural disruption and the formation of the local isolated polar nanoregions [48]. When the NBT amount continues to increase, the appearance of heterophase and the drastic increase of ceramic grains weaken the relaxor characteristic, and ultimately the ΔP value is reduced.

Figure 9c depicts the Weibull distribution of BSZT-xNBT ceramics materials. The Weibull distribution

can be described according to the following equations [44]:

$$X_i = \ln(E_i) \tag{1}$$

$$Y_i = \ln\left(-\ln\left(1 - \frac{i}{1+n}\right)\right), \tag{2}$$

where i, n, and E_i, respectively, represent the serial number, the total number, and the breakdown voltage of tested specimens. It is obvious that all compositions display large β value (> 11). As shown in Fig. 9c, the calculated BDS values of BSZT-xNBT ceramics are 12.01, 16.03, 18.09, and 17.04 kV mm^{-1} for $x = 0.02$, 0.04, 0.06, and 0.08, respectively. The gradually improved BDS may be ascribed to the following two reasons: (1) importantly, the grain size has a reverse correlation on the BDS. The average grain sizes of ceramics are basically equal to the particle size of the powders; (2) the compactness of ceramics plays an indispensable role in the improvement of BDS. The pores of ceramics provide a breakdown path under the applied electric field
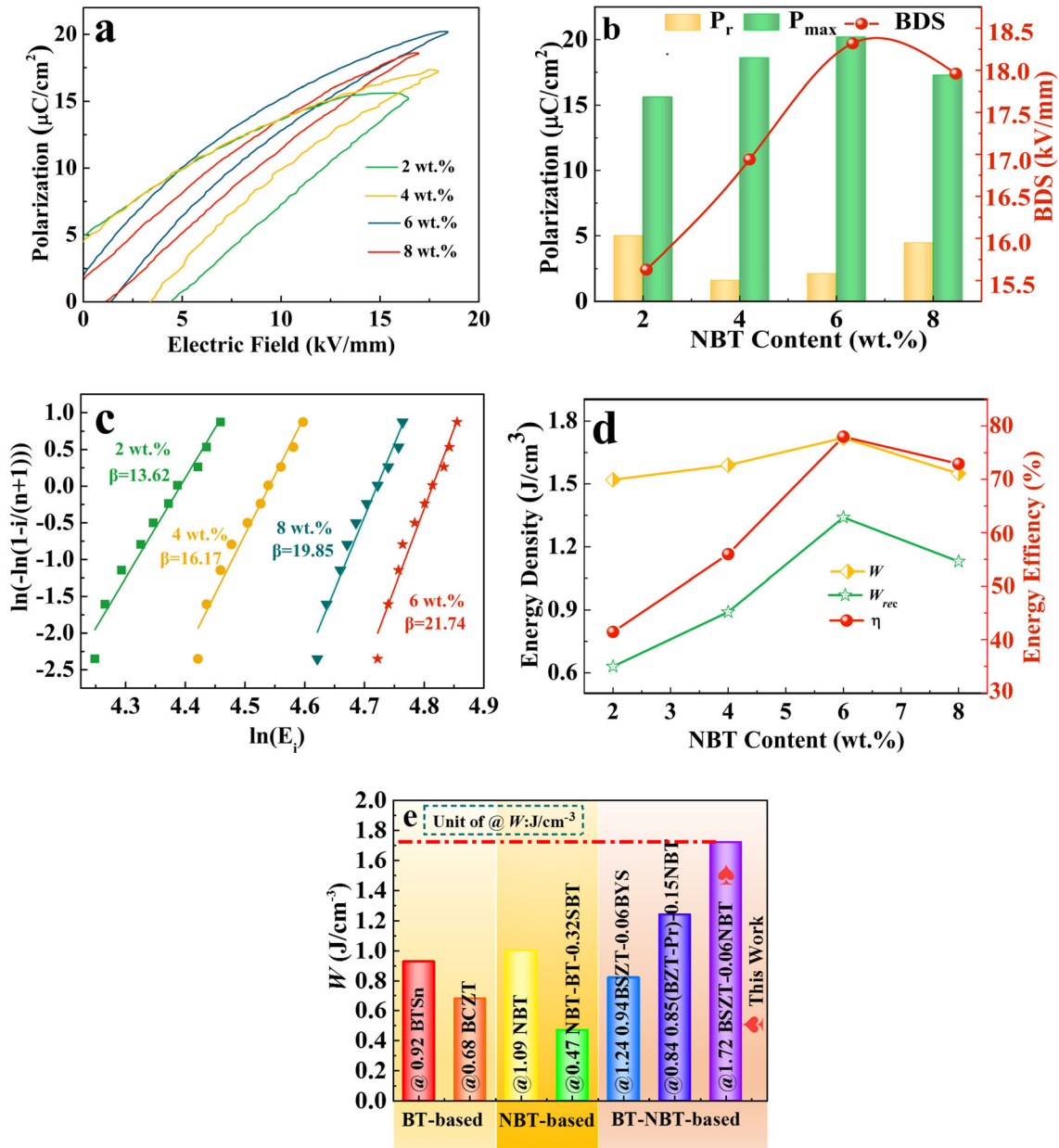
Fig. 9 a Unipolar polarization loops. **b** P_{max}, P_r, and BDS. **c** Weibull distribution function of dielectric breakdown strength. **d** W, W_{rec}, and η of the BSZT-xNBT ceramics as a function of NBT content; **e** comparison of the W of BSZT-0.06NBT ceramics and other lead-free ceramic systems [9,19,49–52]

and increases the heat loss [10]. As a result, for one ceramic, the denser the structure higher the BDS.

The energy storage density and energy storage efficiency of BSZT-xNBT ceramics are calculated using the values of P_m, P_r, and BDS. The highest energy storage density (W, 1.72 J cm^{-3}) and energy storage efficiency η (78.2%) are achieved for the BSZT-0.06NBT ceramics. A comparison of W of BSZT-0.06NBT ceramics and other promising lead-

free bulk ceramics previously reported are presented in Fig. 9c. BSZT-0.06NBT ceramics possess the highest W (1.72 J cm^{-3}), which should be mainly due to their large ΔP value and BDS originated from the existence of polar nanoregions and dense microstructure.

To determine the morphology and composition of domains in the BSZT-xNBT ceramics, we conducted TEM detection. As shown in Fig. 10a and c, large T
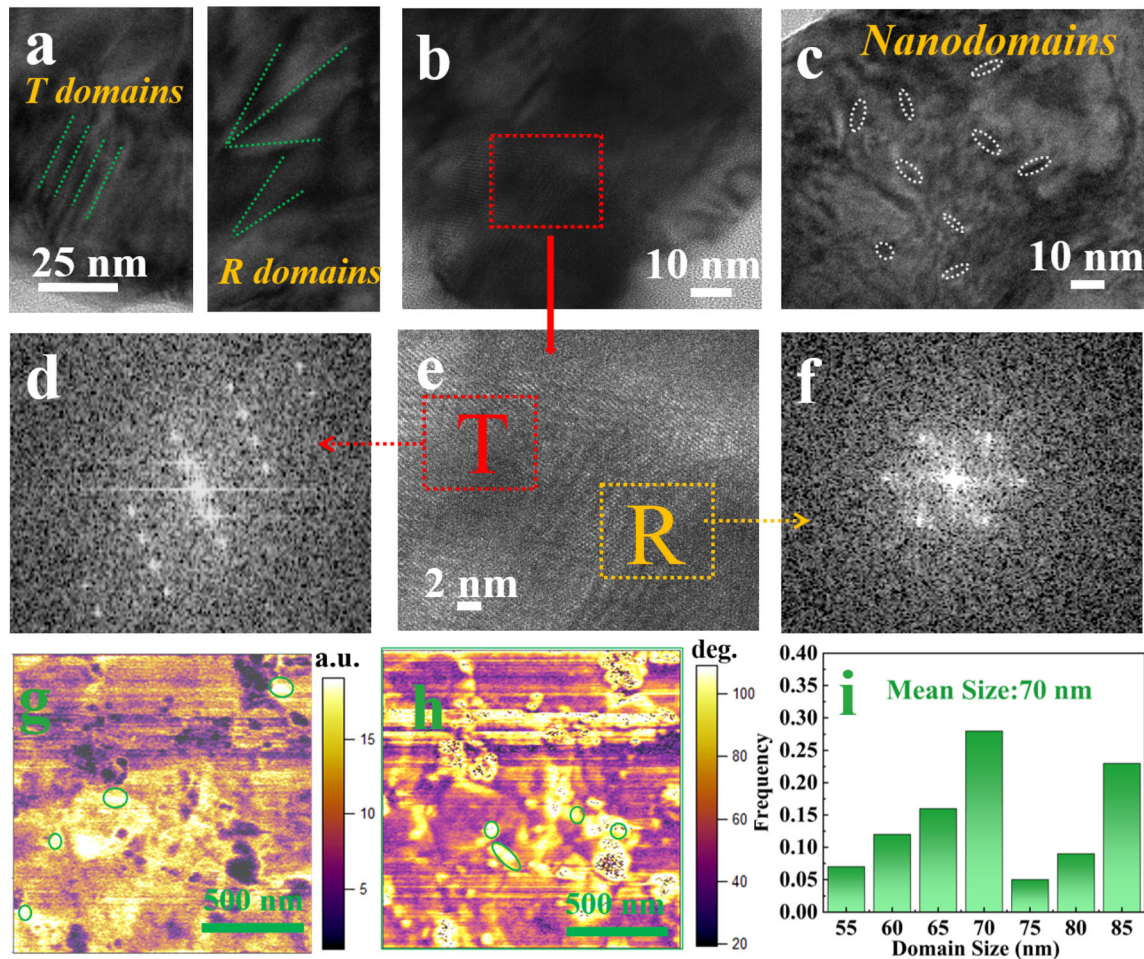
Fig. 10 The morphology and composition of domains in the BSZT-xNBT ceramics revealed by TEM and PFM. **a** Domain morphology in the BSZT-xNBT ceramics ($0 < x < 0.06$). **b** HR-TEM image of BSZT-0.06NBT ceramics. **c** Domain morphology in the BSZT-0.06NBT ceramics. **e** Enlarged TEM image of the red arrow pointing area in (**b**). **d** and **f** FFT patterns transformed from the HR-TEM image. **g** PFM amplitude of the BSZT-0.06NBT ceramics. **h** Phase images of the BSZT-0.06NBT ceramics. **i** Domain size distribution of the BSZT-0.06NBT ceramics

and R phase ferroelectric domains were observed in the BSZT-xNBT ceramics ($0 < x < 0.06$), while BSZT-0.06NBT ceramics owned randomly distributed nanodomains with a size less than 10 nm (Fig. 10b). This indicates that the long-range ordered ferroelectric domains are disrupted into the short-range ordered nanodomains [53]. The obvious local heterostructures were clearly observed in Fig. 10e. Figure 10d and f show the Fast Fourier Transformation (FFT) diagram of the red box area in Fig. 10e. It is proved that the coexistence of R and T phases within the scale of several nano-sized regions could form polar nanoregions. In order to verify the relationship between the domain structure and energy storage properties, PFM measurements were studied. As shown in Fig. 10g and h, the polar nanoregions are detected in

the BSZT-0.06NBT ceramics, which could be ascribed to the introduction of NBT, Bi^{3+} and Na^+ incorporating into the A-site of BSZT lattice leads to the emergence of polar nanoregions [54]. Previous studies revealed that the coexistence of multi-phases and polar nanoregions can promote domain switching because they are easy to respond to the electric field [55]. Moreover, the required response electric field of R phase is lower than that of T phase, and polar nanoregions own small hysteresis loss originated from the presence of their low energy barriers, high dynamics, and enhanced domain wall motion [56, 57]. So, it was highly anticipated that BSZT-0.06NBT ceramics would achieve a better energy storage performance than pure BSZT ceramics.

4 Conclusions

In summary, polar nanoregions and grain refinement engineering were adopted to prepare lead-free BSZT-xNBT relaxor ferroelectric nanoceramics. The significant enhancement in BDS is due to the fine-grained ceramic microstructure, resulting from the introduction of 50 nm NBT. Moreover, it is revealed by PFM and TEM measurements that the introduction of NBT transforms the ferroelectric domains into polar nanoregions, leading to a large ΔP value (18.25 µC cm^{-2}). As a result, a comprehensive W (1.72 J cm^{-3}) and moderate η (78.2%) were obtained in the BSZT-0.06NBT ceramics. This work may provide a new understanding and design for BSZT-NBT-based ceramics with comprehensive energy storage performance for practical dielectric capacitor applications.

Compliance with ethical standards

Conflict of interest The authors declare that they have no conflict of interest.

References

1. J.L. Li, Z.H. Shen, X.H. Chen, S. Yang, W.L. Zhou, M.W. Wang, L.H. Wang, Z. Xu, Nat. Mater. **19**, 1–7 (2020)
2. J. Wang, X.H. Wan, Y. Rao, L. Zhao, K.J. Zhu, J. Eur. Ceram. Soc. **40**, 5589–5596 (2020)
3. Y. Lin, D. Li, M. Zhang, S.L. Zhan, Y.D. Yang, H.B. Yang, Q.B. Yuan, A.C.S. Appl, Mater. Interfaces **11**, 36824–36830 (2019)
4. A. Jain, Y.G. Wang, H. Guo, Ceram. Int. **46**, 24333–24346 (2020)
5. M.Z. Sun, J. Du, C. Chen, P. Fu, P. Li, J.G. Hao, Z.X. Yue, W. Li, Ceram. Int. **46**, 17351–17360 (2020)
6. B.Z. Shen, Y. Li, N.N. Sun, Y. Zhao, X.H. Hao, Nanoscale **12**, 8958–8968 (2020)
7. M. Othmani, A. Amouri, F. Benabdallah, Z. Sassi, L. Lebrun, V. Perrin, Ceram. Int. **46**, 22592–22605 (2020)
8. F. Kang, L. Zhang, L.B. Huang, P. Mao, D.W. Hu, J. Eur. Ceram. Soc. **40**, 1198–1204 (2020)
9. A. Jain, Y.G. Wang, N. Wang, Y. Li, F.L. Wang, J. Physica D **53**, 235301 (2020)
10. A. Jain, Y.G. Wang, H. Guo, N. Wang, Ceram. Int. **46**, 18800–18812 (2020)
11. A. Jain, Y.G. Wang, N. Wang, F.L. Wang, J. Am. Ceram. Soc. **103**, 6308–6318 (2020)
12. N. Qu, H.L. Du, X.H. Hao, J. Mater. Chem. C **7**, 7993–8002 (2019)
13. J.P. Shi, X.L. Chen, X. Li, J. Sun, C.C. Sun, F.H. Pang, H.F. Zhou, J. Mater. Chem. C **8**, 3784–3794 (2020)
14. Y.C. Wu, Y.Z. Fan, N.T. Liu, P. Peng, M.X. Zhou, S.G. Yan, F. Cao, X.L. Dong, G.S. Wang, J. Mater. Chem. C **7**, 6222–6230 (2019)
15. Q. Jin, L.L. Zhao, B. Cui, J. Wang, H.J. Ma, R. Zhang, Y. Liu, X.T. Zhang, J. Mater. Chem. C **8**, 5248–5258 (2020)
16. T. Wang, S.H. Song, Q. Ma, M.L. Tan, J.J. Chen, J. Alloys Compd. **795**, 60–68 (2019)
17. Y. Zhao, J. Du, Z.J. Xu, D.D. Wei, Z.H. Fu, Y.Y. Wang, Mater. Sci. Eng. B **243**, 141–148 (2019)
18. H. Wang, Q. Hu, X. Liu, Ceram. Int. **45**, 23233–23240 (2019)
19. I. Zouari, Z. Sassi, L. Seveyrat, N. Abdelmoula, L. Lebrun, H. Khemakhem, J. Alloys Compd. **825**, 153859 (2020)
20. Y.H. Wang, S.Y. Gao, T. Wang, J.Q. Liu, D. Li, H.B. Yang, G.L. Hu, L. Kong, F. Wang, Ceram. Int. **46**, 12080–12087 (2020)
21. T. Zheng, J.G. Wu, D.Q. Xiao, J.G. Zhu, Prog. Mater. Sci. **98**, 552–624 (2018)
22. M. Peddigari, H. Palneedi, G.T. Hwang, J. Ryu, J. Kor. Ceram. Soc. **56**, 1–23 (2019)
23. X.D. Ren, J. Li, Z.H. Peng, B. Chen, X.S. Qiao, D. Wu, G. Li, H.L. Du, Z.P. Yang, Chem. Eng. J. **390**, 124566 (2020)
24. Z. Sun, L.X. Li, S.H. Kang, X.Y. Chen, L. Si, Dalton Trans. **46**, 14341–14347 (2017)
25. H.Y. Lee, K.H. Cho, H. Nam, Ferroelectrics **334**, 165–169 (2006)
26. M.X. Zhou, R.H. Liang, Z.Y. Zhou, X.L. Dong, J. Mater. Chem. A **6**, 17896–17904 (2018)
27. F. Yang, Z.B. Pan, Z.Q. Ling, D. Hu, J. Ding, P. Li, J.J. Liu, J.W. Zhai, J. Eur. Ceram. Soc. **41**, 2548–2558 (2021)
28. J. Wang, L.L. Zhao, B. Cui, X.T. Zhang, Q. Jin, J. Mater. Sci. Mater. Electron. **31**, 4006–4016 (2020)
29. R. Ma, B. Cui, Y.J. Wang, S.Y. Wang, Y.Y. Wang, Mater. Res. Bull. **111**, 311–319 (2019)
30. H.L. Du, X. Du, H.L. Li, Adv. Appl. Ceram. **112**, 277–282 (2013)
31. Y. Fei, H.B. Yang, Y. Lin, T. Wang, Inorg. Chem. **56**, 13510–13516 (2017)

32. K. Wang, J. Ouyang, M. Wuttig, Y.Y. Zhao, H.B. Cheng, Y. Zhang, R.X. Su, J. Yan, X.L. Zhong, F. Zeng, Adv. Energy Mater. **10**, 2001778 (2020)

33. S. Liu, S.L. Deng, S. Yan, S.Q. Yan, H. Luo, L.L. Yao, L.H. He, Y.H. Li, M.Z. Wu, S.X. Huang, J. Appl. Phys. **122**, 034103 (2017)

34. D.W. Wang, Z.M. Fan, W.B. Li, D. Zhou, A. Feteira, G. Wang, S. Murakami, S.K. Sun, Q.L. Zhao, A.C.S. Appl, Energy Mater. **1**, 4403–4412 (2018)

35. Y.P. Pu, L. Zhang, Y.F. Cui, M. Chen, ACS Sustain. Chem. Eng. **6**, 6102–6109 (2018)

36. M. Benyoussef, M.M. Zannen, J. Belhadi, B. Manoun, J. Dellis, A. Lahmar, Ceram. Int. **46**, 10979–10991 (2020)

37. L. Zhang, Y.P. Pu, M. Chen, J. Alloys Compd. **775**, 342–347 (2017)

38. P. Butnoia, S. Manothama, P. Jaitaa, C. Randornc, G. Ruji-janagula, J. Eur. Ceram. Soc. **38**, 3822–3832 (2018)

39. Q. Li, J. Wang, Y. Ma, L.T. Ma, G.Z. Dong, H.Q. Fan, J. Alloys Compd. **663**, 701–707 (2016)

40. U.D. Venkateswaran, V.M. Naik, R. Naik, Phys. Rev. B **58**, 14256–14260 (1998)

41. D.K. Khatua, G.D. Adhikary, A. Mishra, N. Kumar, A. Senyshyn, S.K. Mishra, S.J. Kim, R. Ranjan, J. Appl. Phys. **127**, 204101 (2020)

42. H.L. Sun, X. Wu, D.F. Peng, K.W. Kwok, A.C.S. Appl, Mater. Interfaces **9**, 34042–34049 (2017)

43. X.J. Xu, J.G. Jiang, H. Ahmad, G.L. Jiang, J. Yin, Z.G. Liu, Ceram. Int. **40**, 11819–11824 (2014)

44. W.G. Ma, P.Y. Fan, D. Salamon, S. Kongparakul, Ceram. Int. **45**, 19895–19901 (2019)

45. Q. Jin, B. Cui, X.T. Zhang, J. Wang, J. Electron. Mater. **50**, 0361–5235 (2021)

46. A. Jan, H.X. Liu, H. Hao, Z.H. Yao, M. Emmanuel, W.G. Pan, A. Ullah, A. Manan, A. Ullah, M.H. Cao, A.S. Ahmad, J. Alloys Compd. **830**, 154611 (2020)

47. Z.T. Chen, X.Y. Bu, B.X. Ruan, J. Du, P. Zheng, L.L. Li, F. Wen, W.F. Bai, W. Wu, L. Zheng, Y. Zhang, J. Eur. Ceram. Soc. **40**, 5450–5457 (2020)

48. X.Y. Zhao, W.F. Bai, Y. Ding, L.J. Wang, S.T. Wu, P. Zheng, J.W. Zhai, J. Eur. Ceram. Soc. **40**, 4475–4486 (2020)

49. S. Merselmiza, Z. Hanania, D. Mezzanea, M. Spreitzerc, A. Bradeškoc, D. Fabijanc, D. Vengustc, M. Amjouda, L. Hajjia, Z. Abkhara, Ceram. Int. **46**, 23867–23876 (2020)

50. V.S. Puli, D.K. Pradhan, D.B. Chrisey, M. Tomozawa, G.L. Sharma, J.F. Scott, R.S. Katiyar, J. Mater. Sci. **48**, 2151–2157 (2013)

51. N.A. Halim, T.S. Velayutham, W.H. Abd. Majid, Ceram. Int. **42**, 15664–15670 (2016)

52. F. Li, K. Yang, X. Liu, J. Zou, J.W. Zhai, B. Shen, P. Li, J. Shen, B.H. Liu, P. Chen, K.Y. Zhao, H.R. Zeng, Scr. Mater. **141**, 15–19 (2017)

53. T.Q. Shao, H.L. Du, H. Ma, S.B. Qu, J. Wang, J. Mater. Chem. A **5**, 554–563 (2017)

54. X. Lv, X.X. Zhang, J.G. Wu, J. Mater. Chem. A **8**, 10026–10073 (2020)

55. H.N. Sun, X.J. Wang, Q.Z. Sun, X.X. Zhang, Z. Ma, M.Y. Guo, B.W. Sun, X.P. Zhu, Q. Liu, X.J. Lou, J. Eur. Ceram. Soc. **40**, 2929–2935 (2020)

56. Z.T. Yang, H.L. Du, L. Jin, Q.Y. Hu, S.B. Qu, Z.N. Yang, Y. Yu, X.Y. Wei, Z. Xu, J. Eur. Ceram. Soc. **39**, 2899–2907 (2019)

57. M.X. Zhou, R.H. Liang, Z.Y. Zhou, X.L. Dong, Inorg. Chem. Front. **6**, 2148–2157 (2019)